J. Mech. Phys. Solids 212 (2026) 106566

Contents lists available at ScienceDirect

Journal of the Mechanics and Physics of Solids

journal homepage: www.elsevier.com/locate/jmps

Programmable mechanical metasurfaces enabled by pre-compressed curved beam architectures

Fan Liu [a,b,d], Zian Jia [c], Xihang Jiang [a], Lifeng Wang [a,*]

[a] Department of Mechanical Engineering, State University of New York at Stony Brook, Stony Brook, NY 11794, USA
[b] Brigham and Women's Hospital, Harvard Medical School, Boston, MA 02115, USA
[c] Department of Ecology and Evolutionary Biology, Princeton University, Princeton, NJ 08544, USA
[d] Center for Nature Inspired Engineering, State University of New York Polytechnic Institute, Utica, NY 13502, USA

ARTICLE INFO

Keywords:
Bistable structures
Curved beams
Snap-through mechanics
Reprogrammable metasurfaces

ABSTRACT

This work presents a comprehensive study of bistability in elastic beams, with a focus on the pre-compressed curved beam as a unique structure exhibiting both tunability and asymmetry in its potential energy landscape. Analytical modeling, supported by finite element simulations and experimental validation, reveals the conditions under which bistability emerges and defines a discriminant surface separating bistable and non-bistable regimes. Unlike conventional bistable systems that rely on lateral loading to overcome energy barriers, the pre-compressed curved beam enables an alternative stable state switching mechanism: the switching is achieved by tuning axial compression to reshape the energy landscape from bistable to non-bistable and back, enabling a controlled stable state transition. Based on this mechanism, a coupled beam design is introduced as a unit cell for constructing programmable 2D metasurfaces. The switching behavior of these units is characterized, and metasurfaces of increasing complexity are demonstrated to achieve diverse and reconfigurable patterns via boundary loading or localized expansion. These findings provide a scalable strategy for shape-programmable mechanical systems with potential applications in soft robotics, adaptive surfaces, and deployable structures.

1. Introduction

Bistability, the ability of a system to adopt two distinct and stable equilibrium states, is a fundamental concept that arises across many areas of physics and engineering, with applications ranging from memory storage (Lisman, 1985), optical switching (Clark and Lagerwall, 1980), and superconducting circuits (Barone and Paterno, 1982), to energy harvesting (Harne and Wang, 2013) and morphing structures (Chen et al., 2018). In mechanical systems, bistability arises from two distinct geometric configurations corresponding to local minima in the elastic energy landscape, such as a buckled beam under axial compression shown in Fig. 1(a). The ability to switch between stable states enables a wide range of functional behaviors (see Fig. 1(b)). Because each equilibrium state is mechanically stable and transitions from one state to another involve large, reversible deformations, bistable structures enable robust shape reconfiguration and have been extensively employed in MEMS for switching and sensing applications (Cao et al., 2020; Huang et al., 2020; Percy and Kanthamani, 2023). In systems where the two stable states differ in potential energy, transitions from the lower to the higher energy state allow mechanical energy to be stored, a mechanism leveraged in energy absorbers for strain energy trapping

* Corresponding author.
E-mail address: lifeng.wang@stonybrook.edu (L. Wang).

https://doi.org/10.1016/j.jmps.2026.106566
Received 15 July 2025; Received in revised form 12 January 2026; Accepted 18 February 2026
Available online 19 February 2026

(Jeong et al., 2019; Ha et al., 2018; Shan et al., 2015). Conversely, transitions from the higher to the lower energy state facilitate rapid energy release, enabling fast actuation and force amplification in soft robotic systems (Chi et al., 2020; Gorissen et al., 2020). These diverse behaviors highlight how tailoring the energy landscape and the switching of stable states of bistable systems can unlock functionalities that extend beyond the capabilities of conventional linear elastic designs.

A wide range of bistable structures and mechanical metamaterials are derived from a core set of fundamental structural elements, including slender beams (Chen et al., 2017; Ghavidelnia et al., 2023; Jia et al., 2020; Li et al., 2017; Liu et al., 2020; Pal and Sitti, 2023; Xia et al., 2020), curved shells (Jia et al., 2022; Liu et al., 2023a, 2023b; Vasios et al., 2021), and origami-inspired geometries (Silverberg et al., 2015; Wang et al., 2024; Yasuda et al., 2022). While shells are particularly suited for three-dimensional shape transformations, and origami enables compact and programmable multistability, slender beams remain the most extensively studied due to their geometric simplicity, analytical accessibility, and tunable bistable behavior (Cao et al., 2021; Chi et al., 2022). Among the various types of beams, double-clamped beams under axial compression exhibit symmetric bistability that can be tuned by adjusting compression and have been used to construct morphable 3D mesostructures capable of reversible shape transformations for reconfigurable microelectronic systems (Fu et al., 2018). Curved beams, in contrast, exhibit bistability without the need for post-fabrication compression, allowing for easier integration into systems that prioritize compactness, fabrication simplicity, or passive actuation. Their inherent curvature gives rise to two stable configurations with distinct potential energy levels, a property that has been effectively utilized in multifunctional soft robotic actuators capable of rapid and programmable shape transformations (Chi et al., 2020). Tilted curved beams are designed to engage higher order bending modes, enabling enhanced elastic energy storage. They have been

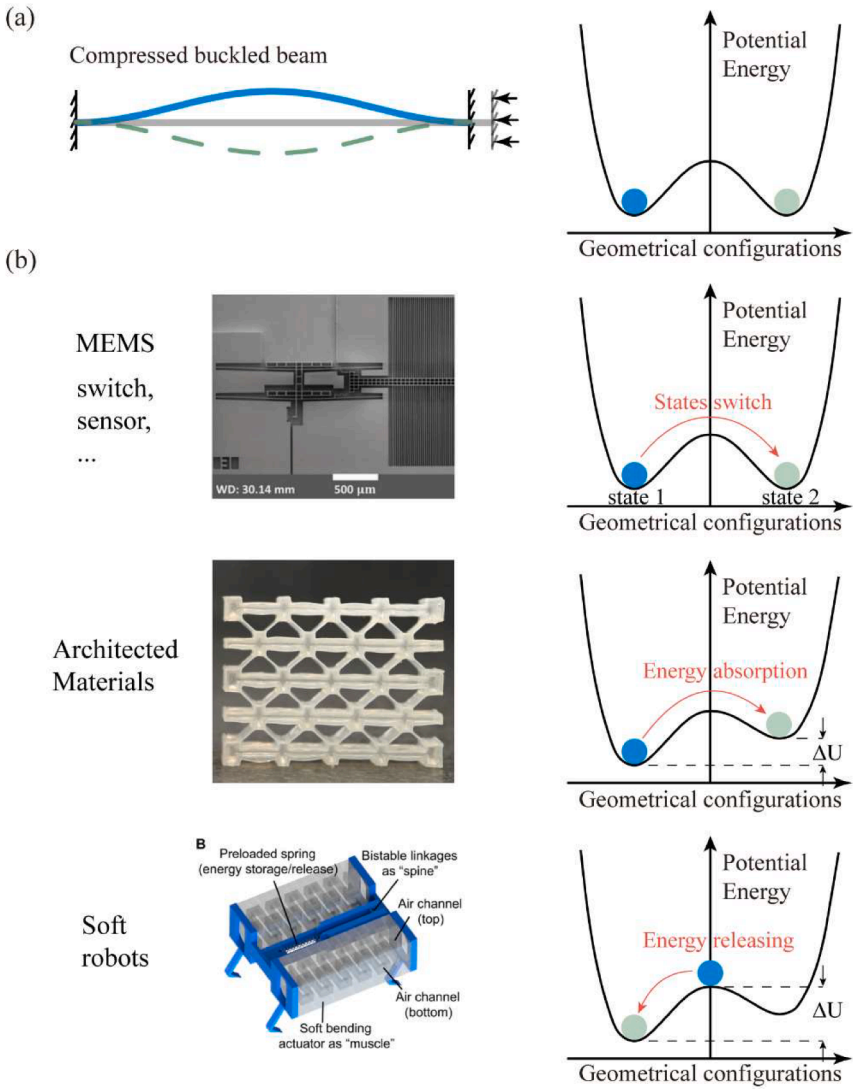

Fig. 1. (a) Schematic of a buckled beam under axial compression and its corresponding potential energy landscape. (b) Representative applications of bistable structures, including microelectromechanical systems (Huang et al., 2020), architected materials for energy absorption (Shan et al., 2015), and soft robotic actuators (Chi et al., 2020).

employed in architected materials to trap strain energy and mitigate impact forces through delayed snap-back behavior (Shan et al., 2015). These functional implementations are grounded in extensive theoretical work that has established the fundamental mechanics governing bistable beams. For compressed buckled beams, analytical models have identified the critical conditions for snap-through and the effects of geometric parameters on stability thresholds (Vangbo, 1998; Vangbo and Bäcklund, 1998). Pre-curved bistable mechanisms have been studied to reveal the role of built-in curvature in shaping asymmetric energy landscapes and stability criteria (Qiu et al., 2004). Furthermore, simplified yet accurate energy-based formulations have been developed to enable rapid design and optimization of bistable structures, offering efficient pathways for engineering complex multistable systems (Yan et al., 2019). More recently, the effects of natural curvature in elastic beams have been systematically analyzed, showing how intrinsic curvature couples bending and twisting responses and leads to rich three-dimensional buckling behaviors (Leanza et al., 2024). In general, bistability in beams is achieved through two approaches: modifying the geometry, such as incorporating pre-curvature, or introducing external constraints, such as axial compression. While analytical descriptions exist for compression-induced and geometry-induced bistability individually, a unified analytical framework that captures their coupled effect remains limited. On the application side, most bistable systems achieve state transitions by applying lateral forces to overcome the energy barrier between stable configurations. For instance, a recent study (Hua et al., 2025) has examined pre-compressed curved beams through lateral force–displacement responses and demonstrated programmable loading and unloading sequences. However, the coupling of axial compression and initial curvature gives rise to a tunable and asymmetric bistability that enables an alternative stable-state switching mechanism, which has not been systematically characterized.

In this study, an analytical framework is established to determine the conditions under which pre-compressed curved beams exhibit bistability, defining the boundary between stable and unstable configurations in the design space. Based on these theoretical results, a compression-driven stable state switching mechanism is uncovered, in which stable state transitions are achieved by tuning the potential energy landscape through axial compression. This mechanism is further applied to the design of coupled-beam unit cells, which are assembled into reprogrammable two-dimensional metasurfaces capable of complex shape transformations, offering a scalable approach for constructing adaptive and programmable mechanical systems for applications in soft robotics and morphing structures.

2. Analytical formulation of bistability in pre-compressed curved beams

This section develops an analytical framework to determine the equilibrium configurations of a curved beam subjected to axial compression, with emphasis on the conditions leading to bistability and the characterization of the corresponding stable shapes. The analytical framework follows the principle of stationary potential energy, where a stable equilibrium configuration corresponds to a shape that yields a local minimum of the total potential energy functional. To clarify the structure of the derivation, the analytical framework is organized into three steps: (i) formulation of the total potential energy, (ii) identification of equilibrium configurations from the first variation of the energy, and (iii) determination of the stability of the equilibrium configurations from the second variation of the energy.

The schematic of a curved beam subjected to axial compression is shown in Fig. 2. The initial shape of the beam is described by

$$y_0(x) = \frac{h}{2}\left(1 - \cos\left(\frac{2\pi x}{l_0}\right)\right), \tag{1}$$

where $h \ll l_0$ is the initial height at the midpoint and l_0 is the initial span length. After compression, the span length shortens to $l = l_0 - d$, where $d \ll l_0$ represents the imposed compression in the x-direction. Assuming the beam has a rectangular cross-section with width b and thickness t, both ends are clamped, satisfying the boundary conditions

$$y(0) = y(l) = y'(0) = y'(l) = 0. \tag{2}$$

While the analysis below is demonstrated for this specific initial shape, the analysis procedure applies more generally to smooth initial shapes satisfying the same boundary conditions. After compression, the deflected shape of the beam is denoted by $y(x)$ and the corresponding total potential energy is expressed as

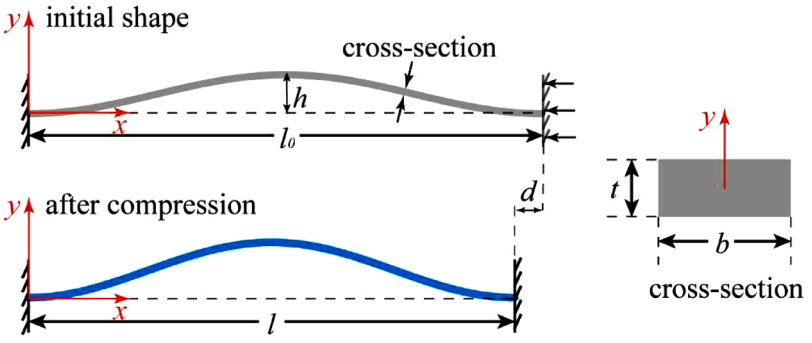

Fig. 2. Schematic of a curved beam subjected to axial compression.

$$u = \frac{EI}{2}\int_0^l \left[y''(x) - y''_0(x)\right]^2 dx + \frac{1}{2}p\cdot(s - s_0), \tag{3}$$

where E is the Young's modulus, $I = bt^3/12$ is the moment of inertia of the cross-section, p is the axial compressive force, s_0 and s denote the arclengths of the beam before and after compression, respectively. To simplify the analysis, the total potential energy is normalized by $EI/l$to obtain its dimensionless form

$$U = \frac{l}{EI}u = \frac{l}{2}\int_0^l \left[y''(x) - y''_0(x)\right]^2 dx + \frac{l}{2EI}p\cdot(s - s_0). \tag{4}$$

The first term represents the bending energy, while the second term corresponds to the axial compression energy. The deformed shape $y(x)$ can be expressed through mode superposition with the buckling modes of a straight clamped–clamped beam as the basis functions. These modes are obtained by solving the equilibrium equation of a straight Euler–Bernoulli beam subjected to an axial compressive load

$$EI\frac{d^4\omega}{dx^4} + p\frac{d^2\omega}{dx^2} = 0, \tag{5}$$

where $\omega(x)$ represents the lateral deflection. Subject to the clamped boundary conditions, the corresponding mode shapes are expressed as:

$$\omega_i = \begin{cases} \left(1 - \cos\left(N_i\frac{x}{l}\right)\right), & N_i = (i+1)\pi \quad i = 1,3,5\ldots \\ \left(1 - \cos\left(N_i\frac{x}{l}\right) + \frac{2}{N_i}\sin\left(N_i\frac{x}{l}\right) - 2\frac{x}{l}\right), & N_i = 2.86\pi, 4.92\pi, 6.94\pi\ldots \quad i = 2,4,6\ldots \end{cases} \tag{6}$$

The detailed derivation of mode shapes is provided in Supporting Information, which are consistent with (Qiu et al., 2004) and (Hua et al., 2025). The shape of the curved beam after compression can be expressed as a linear superposition of these mode shapes:

$$y(x) = \sum_{i=1}^{\infty} A_i\omega_i + y_0. \tag{7}$$

Note that the even modes are antisymmetric and are generally constrained in practical conditions, they are not considered in the present analysis, with $A_i = 0$ for $i = 2,4,6\ldots$. Because the beam shapes of interest correspond to stable equilibrium configurations, which are local minima of the total potential energy, the contribution of higher odd modes ($i = 3,5,7\ldots$) is generally negligible, as they are associated with higher energy states. Therefore, it is often sufficient to approximate the deflection as $y(x) = A_1\omega_1 + y_0$. The third mode is nevertheless included, and the subsequent derivation will show that it does not participate in the stable equilibrium configuration. Considering the superposition of the first and third modes, Eq. (7) can be rewritten as

$$y(x) = \left(A_1 + \frac{h}{2}\right)\left(1 - \cos\left(\frac{2\pi x}{l}\right)\right) + A_3\left(1 - \cos\left(\frac{4\pi x}{l}\right)\right). \tag{8}$$

For simplicity, we define $\widetilde{A}_1 = A_1 + \frac{h}{2}$ in the following analysis. Substituting Eq. (1) and (8) into Eq. (4) gives the first term as

$$\frac{l}{2}\int_0^l \left[y''(x) - y''_0(x)\right]^2 dx = \frac{l}{2}\left(\frac{4\pi^2}{l^2}\right)^2 \int_0^l \left[\left(\widetilde{A}_1 - \frac{h}{2}\right)\cos\frac{2\pi x}{l} + 4A_3\cos\frac{4\pi x}{l}\right]^2 dx. \tag{9}$$

Note that

$$\int_0^l \cos^2\frac{2\pi x}{l}dx = \int_0^l \cos^2\frac{4\pi x}{l}dx = \frac{l}{2}, \int_0^l \cos\frac{2\pi x}{l}\cos\frac{4\pi x}{l}dx = 0, \tag{10}$$

Eq. (9) can be reformulated as

$$\frac{l}{2}\int_0^l \left[y''(x) - y''_0(x)\right]^2 dx = \frac{4\pi^4}{l^2}\left[\left(\widetilde{A}_1 - \frac{h}{2}\right)^2 + 16A_3^2\right]. \tag{11}$$

In the second term in Eq. (4), the axial force p is given by

$$\frac{pl}{Ebt} = s - s_0. \tag{12}$$

The initial arc length s_0 is obtained from the initial shape $y_0(x)$ in Eq. (1), and by neglecting higher-order small terms, it can be

expressed as

$$s_0 = \int_0^{l_0} \sqrt{1 + [y'_0(x)]^2}\,dx \approx l + d + \frac{\pi^2 h^2}{4l}. \tag{13}$$

In a similar manner, the current arc length s is expressed as

$$s = \int_0^{l} \sqrt{1 + [y'(x)]^2}\,dx \approx l + \frac{\pi^2 \widetilde{A}_1^2}{l} + \frac{4\pi^2 A_3^2}{l}. \tag{14}$$

Substituting Eq. (12) and (13) into Eq. (14) gives the second term as

$$\frac{l}{2EI} p \cdot (s - s_0) = \frac{3}{8t^2 l^2}\left(4dl + \pi^2 h^2 - 4\pi^2 \widetilde{A}_1^2 - 16\pi^2 A_3^2\right)^2. \tag{15}$$

The total potential energy is therefore expressed as a function of $\widetilde{A}_1$ andA_3

$$U(\widetilde{A}_1, A_3) = \frac{4\pi^4}{l^2}\left[\left(\widetilde{A}_1 - \frac{h}{2}\right)^2 + 16A_3^2\right] + \frac{3}{8t^2 l^2}\left(4dl + \pi^2 h^2 - 4\pi^2 \widetilde{A}_1^2 - 16\pi^2 A_3^2\right)^2. \tag{16}$$

To determine equilibrium configurations, $\widetilde{A}_1$ and A_3 should satisfy:

$$\frac{\partial U}{\partial \widetilde{A}_1} = \frac{4\pi^4}{l^2}(2\widetilde{A}_1 - h) - \frac{6\pi^2}{t^2 l^2}\widetilde{A}_1\left(4dl + \pi^2 h^2 - 4\pi^2 \widetilde{A}_1^2 - 16\pi^2 A_3^2\right) = 0, \tag{17}$$

$$\frac{\partial U}{\partial A_3} = 32A_3\left[\frac{4\pi^4}{l^2} - \frac{3\pi^2}{4t^2 l^2}\left(4dl + \pi^2 h^2 - 4\pi^2 \widetilde{A}_1^2 - 16\pi^2 A_3^2\right)\right] = 0. \tag{18}$$

The solutions of Eqs. (17) and (18) are classified by the following two discriminants, with detailed derivations provided in the Supporting Information.

$$\Delta_1 = 4\widetilde{p}^3 - 27\widetilde{q}^2, \tag{19}$$

$$\Delta_2 = \frac{dl}{4\pi^2} + \frac{h^2}{18} - \frac{t^2}{3}, \tag{20}$$

where

$$\widetilde{p} = \frac{dl}{\pi^2} + \frac{h^2}{4} - \frac{t^2}{3}, \widetilde{q} = \frac{t^2 h}{6}. \tag{21}$$

Based on the discriminants, Δ_1 and Δ_2, there are four groups of possible solutions:

(I) $\Delta_1 < 0$ and $\Delta_2 < 0$, one solution:

$$(\widetilde{A}_1^I, A_3^I) = \left(\sqrt[3]{\frac{\widetilde{q}}{2} + \sqrt{\frac{\widetilde{q}^2}{4} - \frac{\widetilde{p}^3}{27}}} + \sqrt[3]{\frac{\widetilde{q}}{2} - \sqrt{\frac{\widetilde{q}^2}{4} - \frac{\widetilde{p}^3}{27}}}, 0\right). \tag{22}$$

(II) $\Delta_1 \geq 0$ and $\Delta_2 < 0$, three solutions:

$$(\widetilde{A}_1^{II}, A_3^{II}) = \begin{cases} \left(2\sqrt{\frac{\widetilde{p}}{3}}\cos\left[\frac{1}{3}\arccos\left(\frac{3\widetilde{q}}{2\widetilde{p}}\sqrt{\frac{3}{\widetilde{p}}}\right)\right], 0\right) \\ \left(2\sqrt{\frac{\widetilde{p}}{3}}\cos\left[\frac{1}{3}\arccos\left(\frac{3\widetilde{q}}{2\widetilde{p}}\sqrt{\frac{3}{\widetilde{p}}}\right) - \frac{2\pi}{3}\right], 0\right) \\ \left(2\sqrt{\frac{\widetilde{p}}{3}}\cos\left[\frac{1}{3}\arccos\left(\frac{3\widetilde{q}}{2\widetilde{p}}\sqrt{\frac{3}{\widetilde{p}}}\right) - \frac{4\pi}{3}\right], 0\right) \end{cases}. \tag{23}$$

(III) $\Delta_1 > 0$ and $\Delta_2 \geq 0$, five solutions:

$$(\widetilde{A}_1^{III}, A_3^{III}) = \begin{cases} \left(2\sqrt{\frac{\widetilde{p}}{3}}\cos\left[\frac{1}{3}\arccos\left(\frac{3\widetilde{q}}{2\widetilde{p}}\sqrt{\frac{3}{\widetilde{p}}}\right)\right], 0\right) \\ \left(2\sqrt{\frac{\widetilde{p}}{3}}\cos\left[\frac{1}{3}\arccos\left(\frac{3\widetilde{q}}{2\widetilde{p}}\sqrt{\frac{3}{\widetilde{p}}}\right) - \frac{2\pi}{3}\right], 0\right) \\ \left(2\sqrt{\frac{\widetilde{p}}{3}}\cos\left[\frac{1}{3}\arccos\left(\frac{3\widetilde{q}}{2\widetilde{p}}\sqrt{\frac{3}{\widetilde{p}}}\right) - \frac{4\pi}{3}\right], 0\right) \\ \left(-\frac{h}{6}, \sqrt{\frac{dl}{4\pi^2} + \frac{h^2}{18} - \frac{t^2}{3}}\right) \\ \left(-\frac{h}{6}, -\sqrt{\frac{dl}{4\pi^2} + \frac{h^2}{18} - \frac{t^2}{3}}\right) \end{cases}. \tag{24}$$

(IV) $\Delta_1 < 0$ and $\Delta_2 \geq 0$, however, cannot occur when all geometric parameters are positive real numbers. The corresponding mathematical proof is provided in the Supporting Information.

To determine which configurations are stable, the Hessian matrix of the total potential energy $U(\widetilde{A}_1, A_3)$ is constructed as

$$H(\widetilde{A}_1, A_3) = \begin{pmatrix} U_{\widetilde{A}_1\widetilde{A}_1} & U_{\widetilde{A}_1 A_3} \\ U_{A_3\widetilde{A}_1} & U_{A_3A_3} \end{pmatrix}. \tag{25}$$

With $\Gamma = 4dl + \pi^2h^2 - 4\pi^2\widetilde{A}_1^2 - 16\pi^2A_3^2$, the entries of the Hessian are

$$\begin{aligned} U_{\widetilde{A}_1\widetilde{A}_1} &= \frac{\partial^2 U}{\partial \widetilde{A}_1^2} = \frac{8\pi^4}{l^2} - \frac{6\pi^2}{t^2l^2}\left(\Gamma - 8\pi^2\widetilde{A}_1^2\right) \\ U_{A_3A_3} &= \frac{\partial^2 U}{\partial A_3^2} = \frac{128\pi^4}{l^2} - \frac{24\pi^2}{t^2l^2}\left(\Gamma - 32\pi^2A_3^2\right) \\ U_{\widetilde{A}_1A_3} &= U_{A_3\widetilde{A}_1} = \frac{192\pi^4}{t^2l^2}\widetilde{A}_1A_3 \end{aligned}. \tag{26}$$

The determinant of the Hessian, $\det(H)$, together with $U_{\widetilde{A}_1\widetilde{A}_1}$, determines the nature of each equilibrium configuration:

$$\begin{cases} \det(H) > 0, U_{\widetilde{A}_1\widetilde{A}_1} > 0 & \Rightarrow \text{ local minimum (stable equilibrium)}, \\ \det(H) > 0, U_{\widetilde{A}_1\widetilde{A}_1} < 0 & \Rightarrow \text{local maximum(unstable equilibrium)} \\ \det(H) < 0 & \Rightarrow \text{ saddle point(unstable equilibrium)} \end{cases} \tag{27}$$

For Case I, there is only one equilibrium configuration at $(\widetilde{A}_1^I, A_3^I)$, where $A_3^I = 0$. Eq. (25) yields

$$H(\widetilde{A}_1^I, 0) = \begin{pmatrix} \frac{4\pi^4}{l^2}\left(\frac{h}{\widetilde{A}_1^I} + \frac{12}{t^2}(\widetilde{A}_1^I)^2\right) & 0 \\ 0 & \frac{16\pi^4}{l^2}\left(\frac{h + 6\widetilde{A}_1^I}{\widetilde{A}_1^I}\right) \end{pmatrix}, \tag{28}$$

where $\widetilde{A}_1^I$ is the only real root of the cubic equation

$$g(\widetilde{A}_1) = \widetilde{A}_1^3 - \widetilde{A}_1\left(\frac{dl}{\pi^2} + \frac{h^2}{4} - \frac{t^2}{3}\right) - \frac{t^2h}{6} = 0. \tag{29}$$

Note that $g(0) < 0$ and $g(+\infty) = +\infty$, the real root satisfies $\widetilde{A}_1^I > 0$. Therefore $\det\left[H(\widetilde{A}_1^I, 0)\right] > 0$ and $U_{\widetilde{A}_1\widetilde{A}_1}(\widetilde{A}_1^I, 0) > 0$, indicating a local minimum of U. So $(\widetilde{A}_1^I, 0)$ is a stable equilibrium configuration.

For Case II, there are three equilibrium configurations at $\left(\widetilde{A}_1^{II,i}, A_3^{II,i}\right), i = 1,2,3$, where $A_3^{II,i} = 0$, and $\widetilde{A}_1^{II,i}$ are the three real roots. It can be shown that $\widetilde{A}_1^{II,1} < \widetilde{A}_1^{II,2} < 0 < \widetilde{A}_1^{II,3}$ (see Supporting Information), thus two roots are negative, and one root is positive. Furthermore, the Hessian evaluation yields: (1) For the equilibrium configuration $\left(\widetilde{A}_1^{II,1}, 0\right)$, $\det(H) > 0$ and $U_{\tilde{A}_1\tilde{A}_1} > 0$, which corresponds to a local minimum; (2) For the equilibrium configuration $\left(\widetilde{A}_1^{II,2}, 0\right)$, $\det(H) < 0$, which corresponds to a saddle point; (3) For the equilibrium configuration $\left(\widetilde{A}_1^{II,3}, 0\right)$, $\det(H) > 0$, and $U_{\tilde{A}_1\tilde{A}_1} > 0$, which corresponds to a local minimum.

For Case III, there are five equilibrium configurations at $\left(\widetilde{A}_1^{III,i}, A_3^{III,i}\right), i = 1,2,3,4,5$, where $A_3^{III,1} = A_3^{III,3} = A_3^{III,3} = 0$. Similar to the results discussed in Case II, the following conclusions can be demonstrated: (1) For the equilibrium configuration $\left(\widetilde{A}_1^{III,1}, 0\right)$, $\det(H) > 0$ and $U_{\tilde{A}_1\tilde{A}_1} > 0$, which corresponds to a local minimum; (2) For the equilibrium configuration $\left(\widetilde{A}_1^{III,2}, 0\right)$, $\det(H) > 0$ and $U_{\tilde{A}_1\tilde{A}_1} < 0$, which corresponds to a local maximum; (3) For the equilibrium configuration $\left(\widetilde{A}_1^{III,3}, 0\right)$, $\det(H) > 0$ and $U_{\tilde{A}_1\tilde{A}_1} > 0$, which corresponds to a local minimum as well. More detailed information is provided in the Supporting Information. For the last two equilibrium configurations $\left(\widetilde{A}_1^{III,4}, A_3^{III,4}\right)$ and $\left(\widetilde{A}_1^{III,5}, A_3^{III,5}\right)$, the corresponding Hessian is

$$H\left(\widetilde{A}_1^{III,4}, A_3^{III,4}\right) = H\left(\widetilde{A}_1^{III,5}, A_3^{III,5}\right) = \begin{pmatrix} \frac{\pi^4}{l^2}\left(\frac{4h^2}{3t^2} - 24\right) & -\frac{32\pi^4 h}{t^2 l^2}\sqrt{\frac{dl}{4\pi^2} + \frac{h^2}{18} - \frac{t^2}{3}} \\ -\frac{32\pi^4 h}{t^2 l^2}\sqrt{\frac{dl}{4\pi^2} + \frac{h^2}{18} - \frac{t^2}{3}} & \frac{768\pi^4}{t^2 l^2}\left(\frac{dl}{4\pi^2} + \frac{h^2}{18} - \frac{t^2}{3}\right) \end{pmatrix}. \tag{30}$$

The determinant of the Hessian is

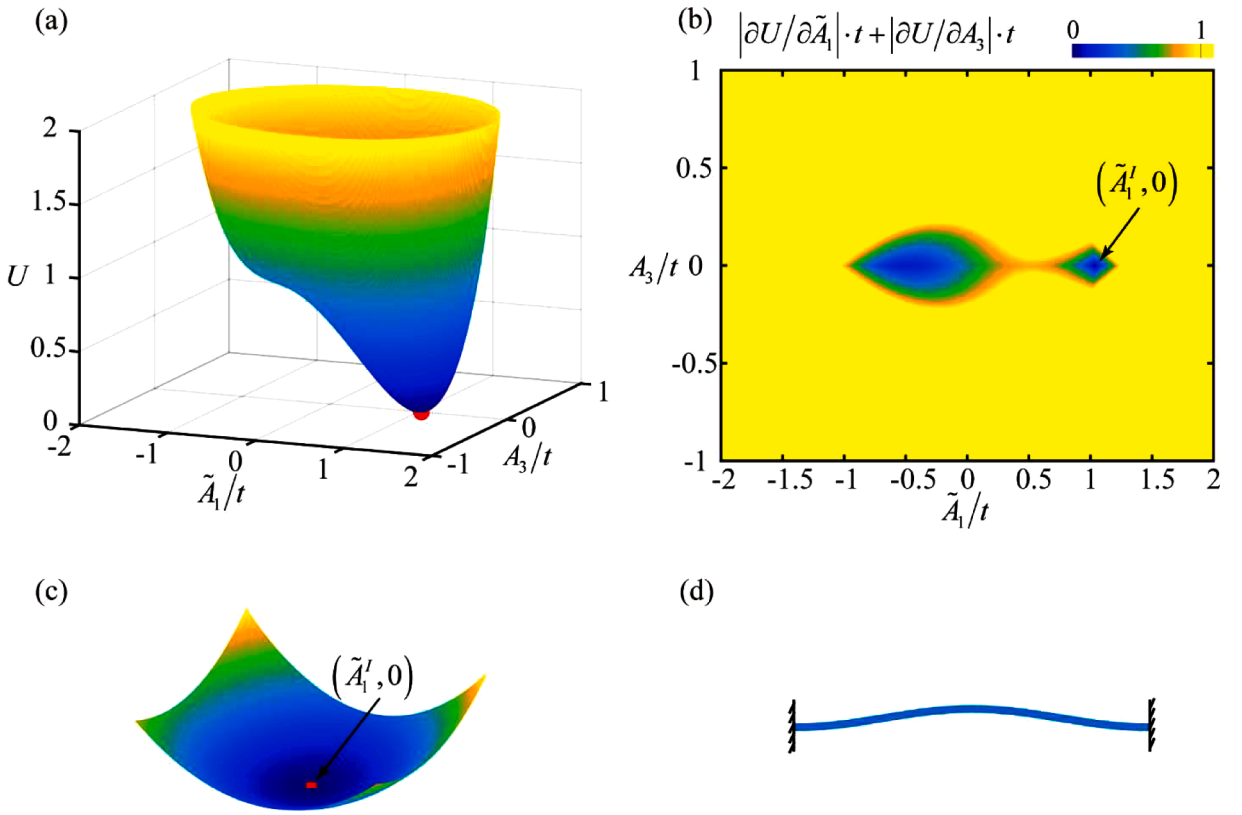

Fig. 3. Energy landscape and equilibrium states for Case I ($\Delta_1 < 0$ and $\Delta_2 < 0$). (a) Total potential energy landscape showing a single potential well. (b) Normalized first derivative $|\partial U/\partial \widetilde{A}_1| \cdot t + |\partial U/\partial A_3| \cdot t$, where the single zero point is observed at $(\widetilde{A}_1^I, 0)$. (c) Local energy surface near $(\widetilde{A}_1^I, 0)$, confirming a local minimum. (d) The corresponding beam shape at the equilibrium state.

$$\det\left[H\left(\tilde{A}_1^{III,4},A_3^{III,4}\right)\right]=\det\left[H\left(\tilde{A}_1^{III,5},A_3^{III,5}\right)\right]=-\frac{18432\pi^8}{t^2l^4}\left(\frac{dl}{4\pi^2}+\frac{h^2}{18}-\frac{t^2}{3}\right)<0, \tag{31}$$

indicating that both are saddle points.

To verify the analytical results, three representative cases are examined. All cases share the same parameters $h/t=2.0$ and $l/t=40$, while the imposed compressions are $d/l=0.0005$, 0.002, and 0.004, corresponding to Cases I, II, and III, respectively.

For Case I ($\Delta_1<0$ and $\Delta_2<0$), the potential energy landscape shown in Fig. 3(a) exhibits a single potential well with only one equilibrium configuration. The normalized first-derivative contour in Fig. 3(b) reveals a single zero point, corresponding to the unique equilibrium at $\left(\tilde{A}_1^{I},0\right)$. The local energy landscape near this point, shown in Fig. 3(c), confirms that it represents a strict local minimum. Fig. 3(d) illustrates the beam shape at this equilibrium configuration.

For Case II ($\Delta_1\geq 0$ and $\Delta_2<0$), the potential energy landscape shown in Fig. 4(a) exhibits two stable equilibrium states. The normalized first derivative contour in Fig. 4(b) reveals three zero points, corresponding to three equilibrium states. The local energy landscapes near these three points, shown in Fig. 4(c), confirm that $\left(\tilde{A}_1^{II,1},0\right)$ and $\left(\tilde{A}_1^{II,3},0\right)$ represent two local minima, while $\left(\tilde{A}_1^{II,2},0\right)$ represents a saddle point. The corresponding beam shapes for these three equilibria are illustrated in Fig. 4(d) respectively.

For Case III ($\Delta_1\geq 0$ and $\Delta_2\geq 0$), the potential energy landscape shown in Fig. 5(a) exhibits two stable equilibrium states. The normalized first derivative contour in Fig. 5(b) shows five zero points, corresponding to the equilibrium configurations. The local energy landscapes near these five points, shown in Fig. 5(c), confirm that $\left(\tilde{A}_1^{III,1},0\right)$ and $\left(\tilde{A}_1^{III,3},0\right)$ represent two local minima, $\left(\tilde{A}_1^{III,2},0\right)$ is a local maximum, and $\left(\tilde{A}_1^{III,4},A_3^{III,4}\right)$ and $\left(\tilde{A}_1^{III,5},A_3^{III,5}\right)$ are two saddle points. The corresponding beam shapes for these five

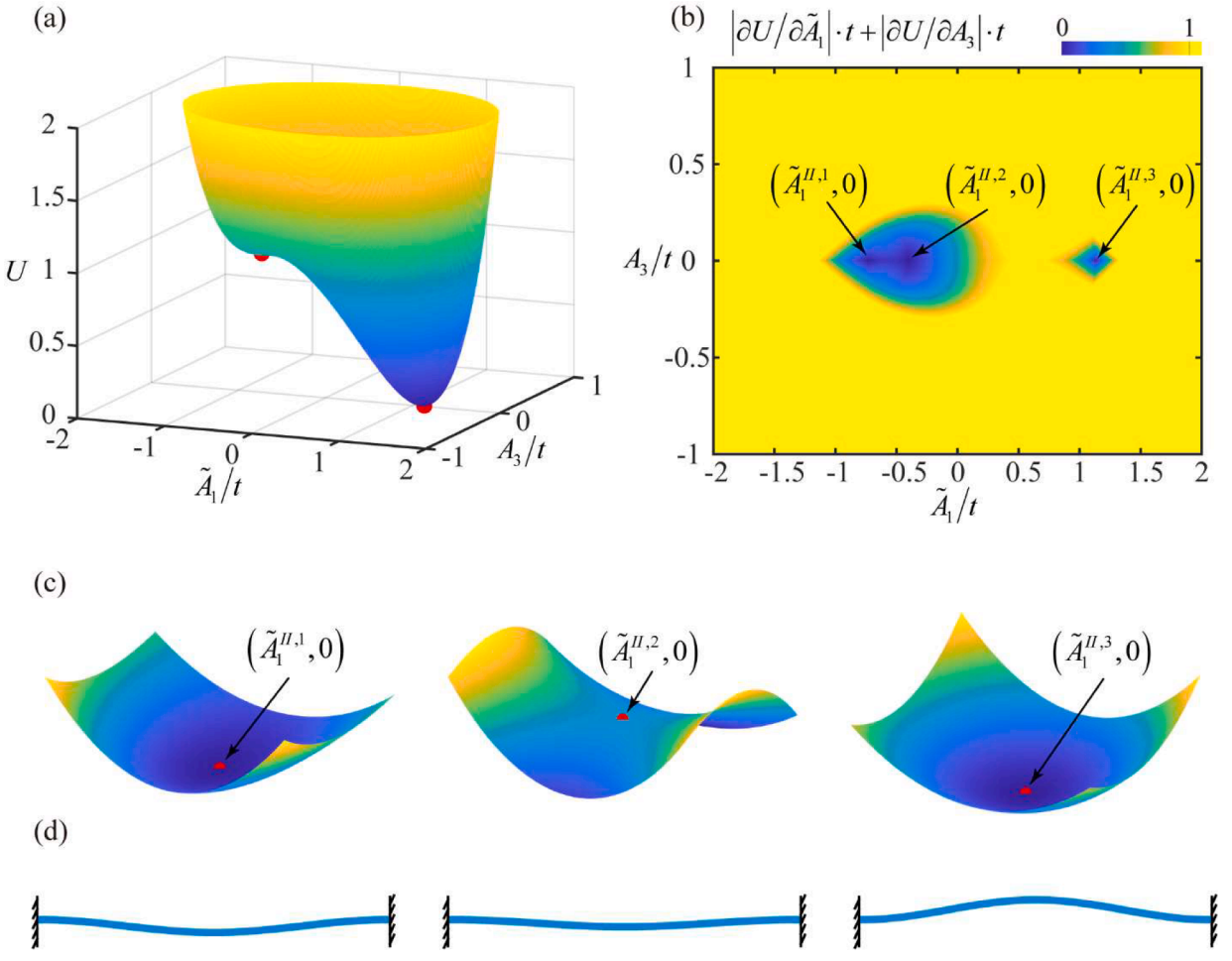

Fig. 4. Energy landscape and equilibrium states for Case II ($\Delta_1\geq 0$and$\Delta_2<0$). (a) Total potential energy landscape. (b) Normalized first derivative $|\partial U/\partial\tilde{A}_1|\cdot t+|\partial U/\partial A_3|\cdot t$, where three zero points are observed. (c) Local energy surfaces, confirming $\left(\tilde{A}_1^{II,1},0\right)$ and $\left(\tilde{A}_1^{II,3},0\right)$represent two local minima, while $\left(\tilde{A}_1^{II,2},0\right)$ is a saddle point. (d) Corresponding beam shapes at the three equilibrium states.

equilibria are illustrated in Fig. 5(d).

The results show that $A_3 = 0$ at all stable configurations and Δ_1 alone governs the bistability of the curved beam under axial compression. The bistable behavior is comprehensively characterized by three dimensionless parameters h/t, l/t, and d/l. Fig. 6(a) shows that Δ_1 forms a dome-shaped surface. Five cross-sections of this surface, corresponding to different values of $l/t = 20 \sim 60$, are plotted in Fig. 6(b) to illustrate how these parameters influence bistability. First, beams with larger l/t values exhibit wider bistable regions; in other words, if a beam is bistable for a certain l/t, it will also be bistable for any larger l/t. Second, there exists a critical value of h/t, corresponding to the peaks of the cross-sectional curves, such that either increasing or decreasing h/t beyond this value can lead to bistability. Third, any beam with $h/t \geq 4/\sqrt{3}$ is always bistable. In the recent study by (Hua et al., 2025), the bistability of pre-compressed curved beams has been analyzed using the dimensionless axial force as a control variable. Their theoretical framework provides valuable physical insight; however, during deformation the axial force generally varies in a non-monotonic manner, such that a given force level may correspond to multiple displacement states. In contrast, the applied axial displacement is a prescribed and fixed boundary condition in practical implementations, leading to a single-valued and well-defined parameterization of the stability criterion.

To better understand the emergence of bistability, the normalized first derivative $|\partial U/\partial \widetilde{A}_1| \cdot t$ is shown in Fig. 7 (a–d) for $l/t = 40$, d/l ranging from 0 to 0.005 and h/t from 1.0 to 2.5. Note that A_3 is set to zero because the previous analysis concludes that A_3 does not contribute to the stable states. From Fig. 7, it can be observed that as the initial curvature h/t increases, the compression d/l to achieve bistability decreases. For beams with small initial curvature, relatively large compression is necessary to induce bistability, as shown in Fig. 7(a), whereas beams with sufficiently large initial curvature are inherently bistable even without compression, as shown in Fig. 7(d).

We next examine two limiting cases. For a double-clamped straight beam ($h = 0$), Eq. (16) simplifies to

$$U(\widetilde{A}_1) = \frac{4\pi^4}{l^2}\widetilde{A}_1^2 + \frac{6}{t^2 l^2}\left(dl - \pi^2 \widetilde{A}_1^2\right)^2. \tag{32}$$

By varying the normalized axial compression d/l, the corresponding potential energy profiles are shown in Fig. 8(a). For small compression, the potential energy exhibits a single U-shaped well, indicating no bistability. As d/l increases, the energy landscape

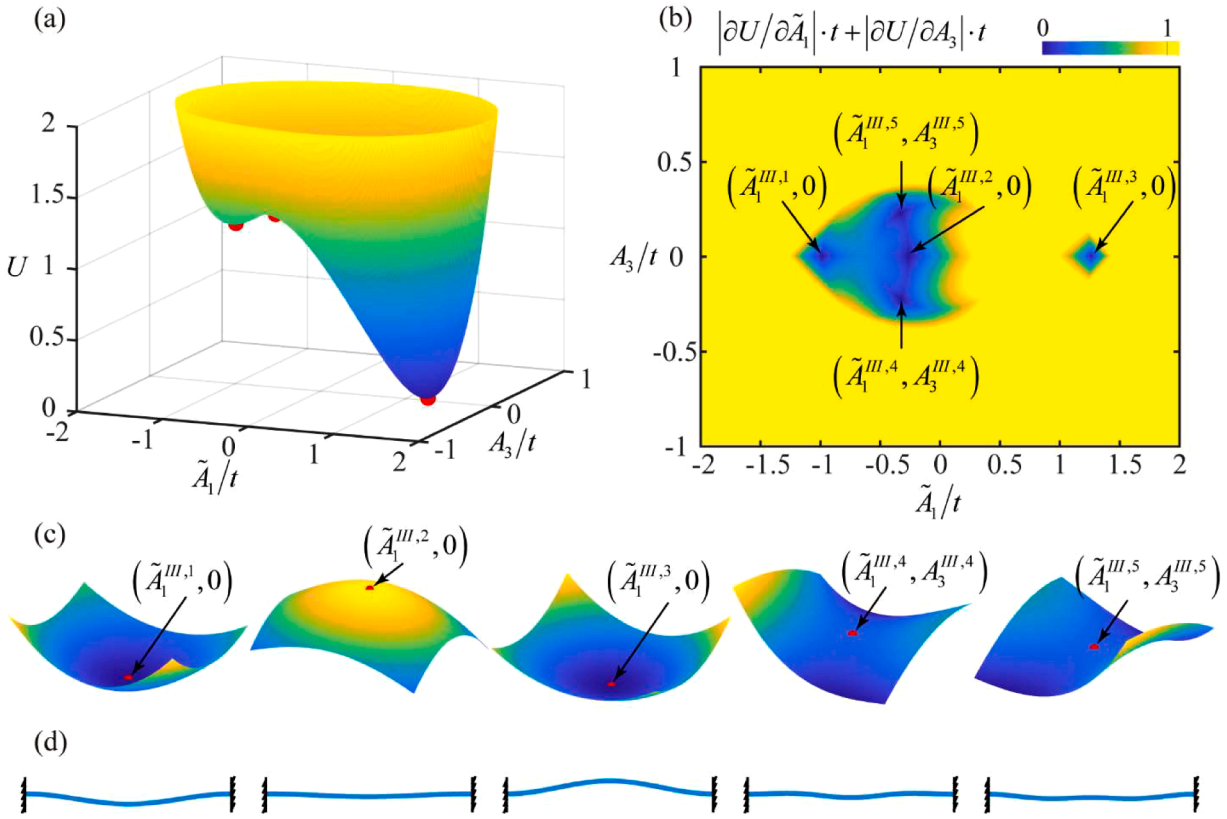

Fig. 5. Energy landscape and equilibrium states for Case III ($\Delta_1 \geq 0$ and $\Delta_2 \geq 0$). (a) Total potential energy landscape showing two stable equilibrium states. (b) Normalized first derivative $|\partial U/\partial \widetilde{A}_1| \cdot t + |\partial U/\partial A_3| \cdot t$, where five zero points are observed. (c) Local energy surfaces confirming that $\left(\widetilde{A}_1^{III,1}, 0\right)$ and $\left(\widetilde{A}_1^{III,3}, 0\right)$ represent two local minima, $\left(\widetilde{A}_1^{III,2}, 0\right)$ is a local maximum, but $\left(\widetilde{A}_1^{III,4}, A_3^{III,4}\right)$ and $\left(\widetilde{A}_1^{III,5}, A_3^{III,5}\right)$ are two saddle points. (d) Corresponding beam shapes at the five equilibrium states.

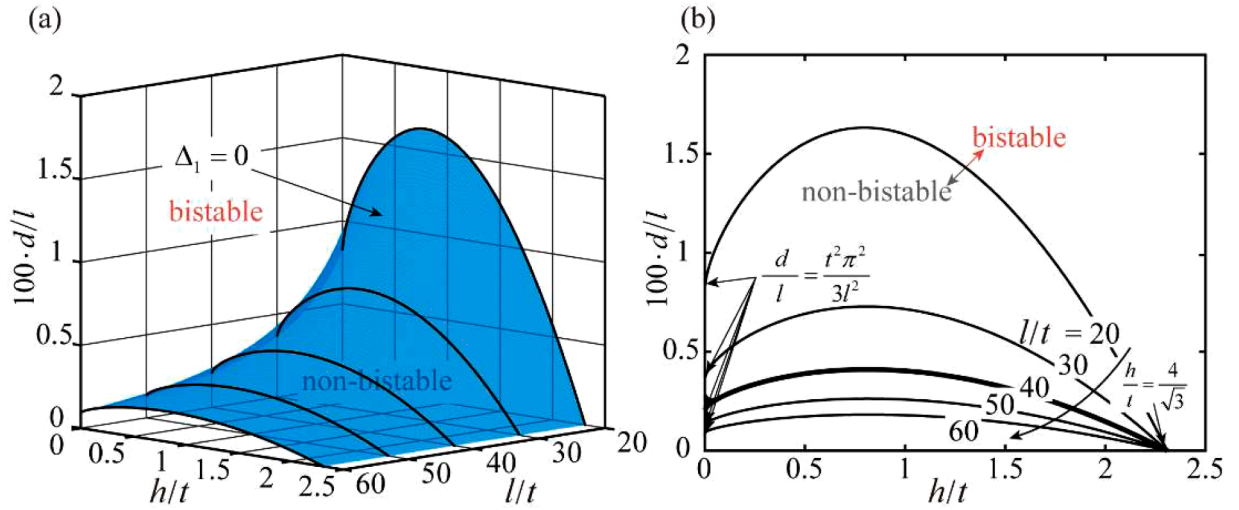

Fig. 6. (a) Dome-shaped surface of Δ_1 that defines the bistable regime in the design space of compressed curved beams. (b) Five representative cross-sections of the Δ_1 surface. A beam is bistable if its corresponding parameter set lies above the surface and non-bistable if it lies below.

transitions from a U-shape to a W-shape, signifying the emergence of two equilibrium states. The evolution of $|\partial U/\partial \widetilde{A}_1| \cdot t$ in Fig. 8(b) further shows this transition. Initially, only one equilibrium exists at $\widetilde{A}_1 = 0$, corresponding to the straight, unbuckled beam. When d/l exceeds a critical value, three equilibrium states appear: one unstable straight state ($\partial^2 U/\partial \widetilde{A}_1^2 < 0$) and two stable buckled states ($\partial^2 U/\partial \widetilde{A}_1^2 > 0$). The critical compression, marking the onset of bistability, is

$$\frac{d_{cr}}{l} = \frac{t^2\pi^2}{3l^2}, \tag{33}$$

which corresponds to the classical buckling limit. Expressed in terms of force, the critical load is $P_{cr} = d_{cr}/l \cdot Etb = 4\pi^2 EI/l^2$ (Timoshenko and Gere, 2012).

The second limiting case, a double-clamped curved beam with no compression ($d = 0$), Eq. (16) simplifies to

$$U(\widetilde{A}_1) = \frac{4\pi^4}{l^2}\left[\left(\widetilde{A}_1 - \frac{h}{2}\right)^2\right] + \frac{3}{8t^2l^2}\left(\pi^2 h^2 - 4\pi^2 \widetilde{A}_1^2\right)^2. \tag{34}$$

The normalized curvature h/t governs bistability. As shown in Fig. 9(a), for small h/t, the potential energy has a single minimum at positive $\widetilde{A}_1$. Increasing h/t introduces a second minimum in the negative $\widetilde{A}_1$ region, as illustrated by $|\partial U/\partial \widetilde{A}_1| \cdot t$ in Fig. 9(b). The critical curvature separating non-bistable and bistable behavior is

$$\frac{h}{t} = \frac{4}{\sqrt{3}}, \tag{35}$$

which is consistent with pervious results (Qiu et al., 2004).

For the compressed straight beam, the potential energy expression, Eq. (32), is a function of $\widetilde{A}_1^2$, resulting in a symmetric energy profile about $\widetilde{A}_1 = 0$. In this case, the two stable equilibrium positions have identical potential energy values. Moreover, since the potential energy depends on the axial compression d, the bistable behavior can be tuned by adjusting the axial compression. Therefore, the compressed straight beam exhibits symmetric and tunable bistability. In contrast, the curved beam's potential energy contains a linear $\widetilde{A}_1$ term in Eq. (34), which breaks the symmetry of the energy profile. Here, one stable position corresponds to the as-fabricated (zero energy) state, while the other represents a local energy minimum with a nonzero potential. The bistability of the curved beam is an inherent property defined by its initial shape and cannot be tuned after fabrication, resulting in inherently asymmetric bistability.

The pre-compressed curved beam, however, represents a more complex and versatile system. Its bistability is governed by both the compression and the initial curvature, giving rise to a tunable and asymmetrical bistability. For both the compressed straight beam and the curved beam, transitioning between stable states requires external energy input to overcome the energy barrier separating the equilibria. However, in the case of the compressed curved beam, the tunable and asymmetrical nature of the potential energy offers alternative mechanisms for stable state switching. This property underpins the fundamental mechanism for designing programmable metasurfaces, which will be discussed in Section 4.

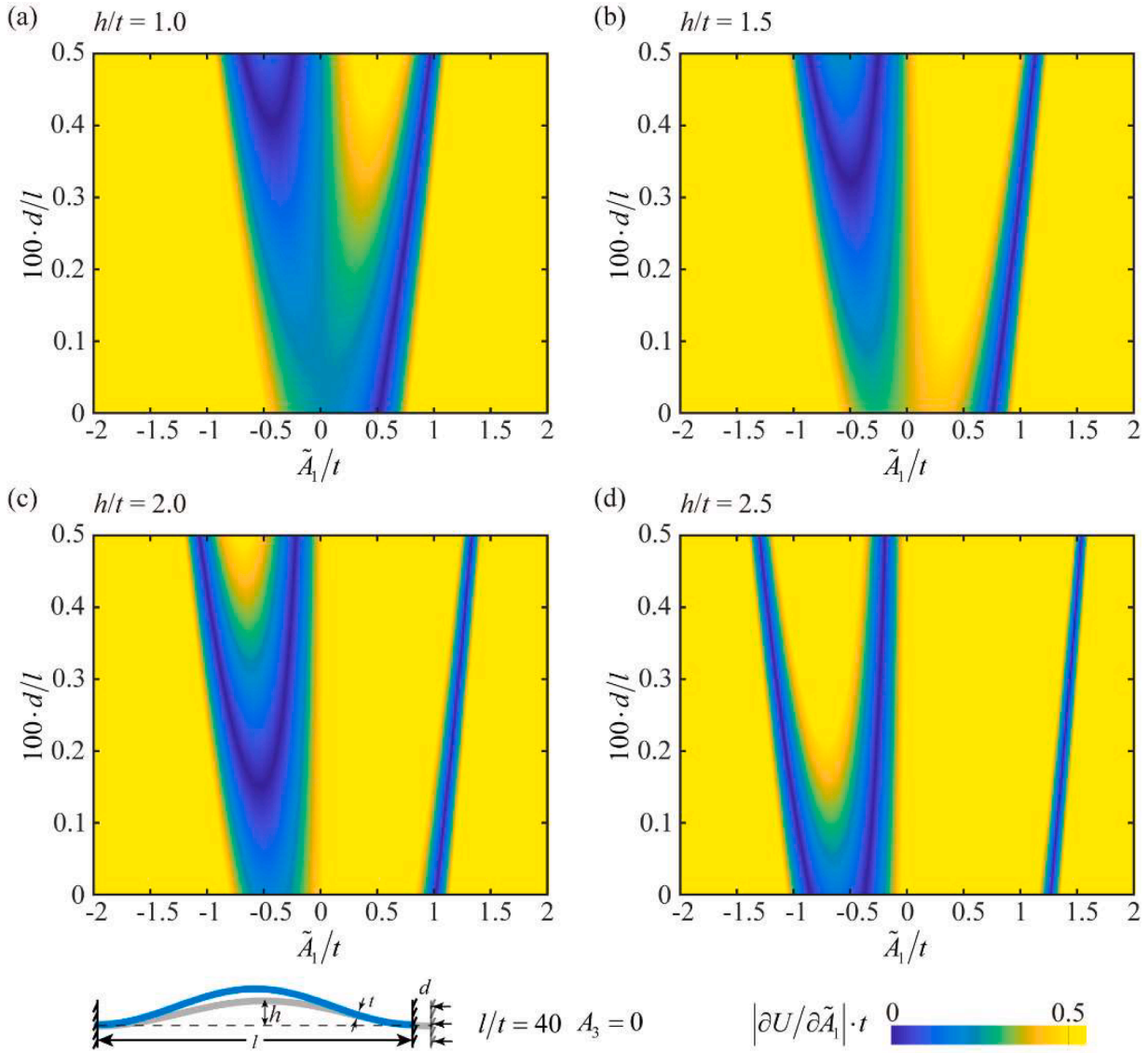

Fig. 7. $|\partial U/\partial \tilde{A}_1| \cdot t$of the beams with varying normalized compression d/l and normalized initial curvature h/t.

3. Numerical and experimental evaluation of stability regimes

To further verify the analytical solution, a nonlinear finite element analysis is conducted using ABAQUS. The beam is modeled using Timoshenko beam elements (B21) with the following geometrical and material properties: $l = 40$ mm, $b = 5$ mm, $t = 1$ mm, $E = 2000$ MPa, and $\nu = 0.3$. Both translational and rotational degrees of freedom are fully constrained at the end nodes to ensure zero displacement and zero slope, while an additional rotational constraint is applied at the beam's midpoint to suppress the second mode, consistent with the analytical assumption. The mesh comprises 100 elements along the beam, and a convergence study verifies that this discretization is sufficient to accurately capture the deformation modes and force responses of interest. The analysis consists of two sequential steps: in Step 1, an axial displacement is applied at the beam ends to achieve a prescribed compression; in Step 2, a lateral displacement is introduced at the beam's midpoint to initiate snap-through and measure the corresponding reaction force. Geometric nonlinearity is also included in all simulation steps to accurately capture large deformation behavior and snap-through responses. The results are used to extract force–displacement curves and assess bistability, providing quantitative comparison with the theoretical predictions. The lateral displacement is applied at the center of the beam, as shown in Fig. 10(a), and the resulting force–displacement curves are obtained. A force–displacement curve with a single intersection at the x-axis corresponds to a non-bistable case, while three intersections indicate bistability.

A set of normalized force–displacement curves for beams with $l/t = 40$, $h/t = 0.5$, and $100 \cdot d/l$ ranging from 0 to 0.6 are shown in Fig. 10(c). The first 20 curves with $100 \cdot d/l < 0.4$ (in gray) each have only one intersection with the x-axis at the origin, indicating that

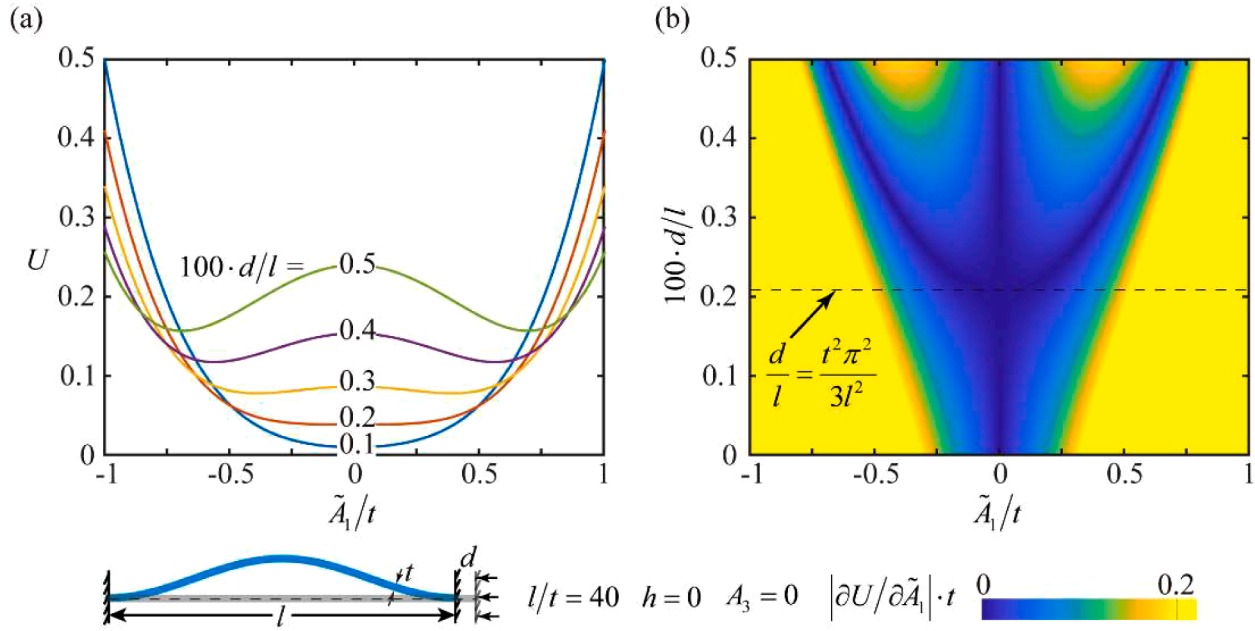

Fig. 8. (a) Potential energy profile of the compressed beam under varying compression d/l. (b) $|\partial U/\partial\tilde{A}_1|\cdot t$ of the compressed beam under varying compression d/l.

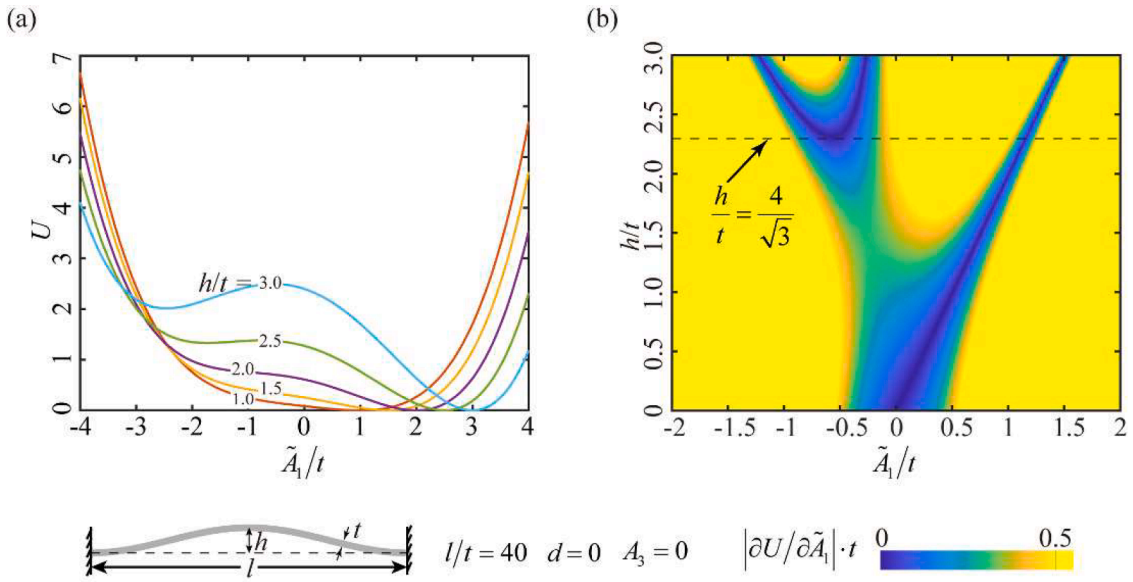

Fig. 9. (a) Potential energy profile of the curved beam under varying initial curvature h/t. (b) $|\partial U/\partial\tilde{A}_1|\cdot t$ of the curved beam under varying initial curvature h/t.

these beams are non-bistable. In contrast, the following 11 curves with $100\cdot d/l \geq 0.4$ (in red) have three intersections with the x-axis, demonstrating bistable behavior. These 31 curves correspond to the column of 31 dots at $h/t = 0.5$ as shown in Fig. 10(b), where bistable beams are marked with red dots and non-bistable beams are marked with gray dots. Following the same procedure, a series of 279 simulations are conducted with $l/t = 40$, h/t ranging from 0.25 to 2.25, and $100\cdot d/l$ ranging from 0 to 0.6 to determine the bistability of the beams. The corresponding force–displacement curves are shown in Fig. 10(c–f), and the bistability results are presented in Fig. 10(b). The plane shown in Fig. 10(b) corresponds to the cross-sectional plane at $l/t = 40$in Fig. 6(a). This cross-section intersects the discriminant surface along a curve, representing the analytical boundary that separates bistable and non-bistable beams. The analytical boundary curve is overlaid in Fig. 10(b), where it aligns closely with the division between the red (bistable) and gray

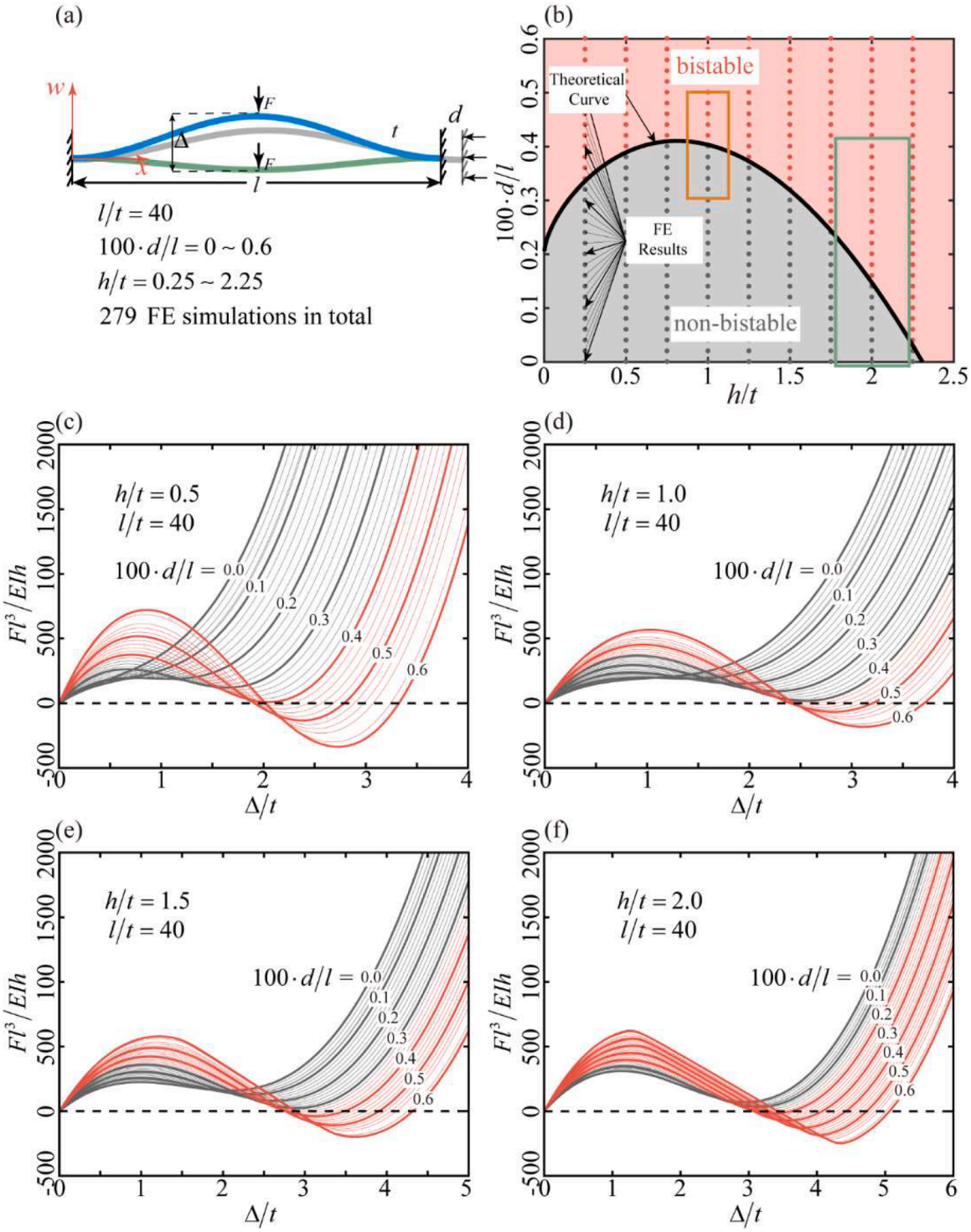

Fig. 10. (a) Schematic of the finite element model showing the geometry, boundary conditions, and loading procedure used to assess the bistability of pre-compressed curved beams. (b) Comparison between finite element simulation results and the theoretical discriminant curve for beams with varying initial curvature and compression. (c-f) Normalized lateral force–displacement curves obtained from FE simulations for different combinations of initial curvature and axial compression, demonstrating transitions between bistable and non-bistable behavior.

(non-bistable) dots, clearly separating the upper bistable region from the lower non-bistable region. The analytical results show excellent agreement with the simulation results.

Experimental tests are conducted to further validate the analytical predictions of the bistable behavior of pre-compressed curved beams. Specimens are fabricated using an Anycubic Photon M3 Plus SLA 3D printer with commercial photopolymer resin, which offers a high printing resolution of 34 μm in the XY plane and 10 μm in the Z direction, ensuring precise fabrication of both the beam geometry and the integrated adjustable boundary feature, which includes a 100 μm gap to accommodate controlled axial compression. The fabricated 3D printed beam has the following geometrical and material properties: $l = 100$ mm, $h = 5$ mm, $t = 2.5$ mm, $E = 800$ MPa, and $\nu = 0.3$. Each specimen incorporates custom-designed adjustable boundary fixtures that allow controlled tuning of axial end compression by inserting precision metal shims, as shown in Fig. 11(a). The lateral force–displacement response is measured using a universal testing machine (MTS Criterion® Electromechanical Test System) equipped with a 100 N load cell. Lateral displacement is applied at the beam midpoint using a clamping fixture that also constrains rotation, thereby suppressing second modes. A loading rate of 0.02 mm/s is used to maintain quasi-static conditions.

In the test, each specimen has $l/t = 40$, $h/t = 2.0$, and $100 \cdot d/l$ ranging from 0 to 0.4, corresponding to the region enclosed by the green box in Fig. 10(b). The testing procedure consisted of two steps: first, an initial compression d is applied using adjustable boundaries; second, a displacement-controlled load is applied at the beam center, pushing it downward quasi-statically. For five different initial compressions, five force–displacement curves are measured, and the normalized results are shown in Fig. 11(b). Of these, the curves for $100 \cdot d/l = 0.0$ and 0.1 each had a single intersection with the x-axis, indicating non-bistable behavior, while the other three ($100 \cdot d/l = 0.2$, 0.3, and 0.4) had three intersections, indicating bistability. Fig. 11(c) shows the analytical boundary curve separating the bistable and non-bistable regions, along with the experimental results, where red and gray dots indicate bistable and non-bistable samples, respectively. The experimental results match the analytical predictions closely, further confirming the validity of the analytical solution.

4. Mechanism of compression-driven stable state switching

Conventionally, transitions between stable states are achieved by applying a lateral force to overcome the energy barrier separating the two states, which does not require geometric pre-curvature. In contrast, the axial compression–driven switching mechanism considered here relies on geometric asymmetry to selectively eliminate one stable state. As a result of this geometric asymmetry, the compressed curved beam exhibits two stable states with different potential energies: the lower-energy configuration is referred to as the primary stable state, while the higher-energy configuration is the secondary stable state. This section focuses on the mechanisms governing transitions between these two states.

For a representative case with $l/t = 40$, $h/t = 1.0$ and $100 \cdot d/l = 0.45$, the beam is bistable since the critical compression required for bistability is approximately $100 \cdot d/l \approx 0.4$, as highlighted in the orange box in Fig. 10(b) and shown in Fig. 12(a). The shapes of the beam at the primary and secondary stable states are shown in Fig. 12(b), with the primary state (blue) bent upward and the secondary state (green) bent downward. Switching from the primary to the secondary stable state can be achieved by applying a downward lateral displacement at the center of the beam. The corresponding force–displacement curve is shown in Fig. 12(b). By supplying external energy, the system overcomes the energy barrier and transitions to the secondary state. Switching from the secondary back to the primary stable state can be achieved in two ways. The first method mirrors the previous process: a lateral displacement is applied in the opposite direction, allowing the system to cross a smaller energy barrier and return to the primary state. The associated reaction force–displacement curve is the same as before but in the opposite direction, as indicated by the black arrows in Fig. 12(b).

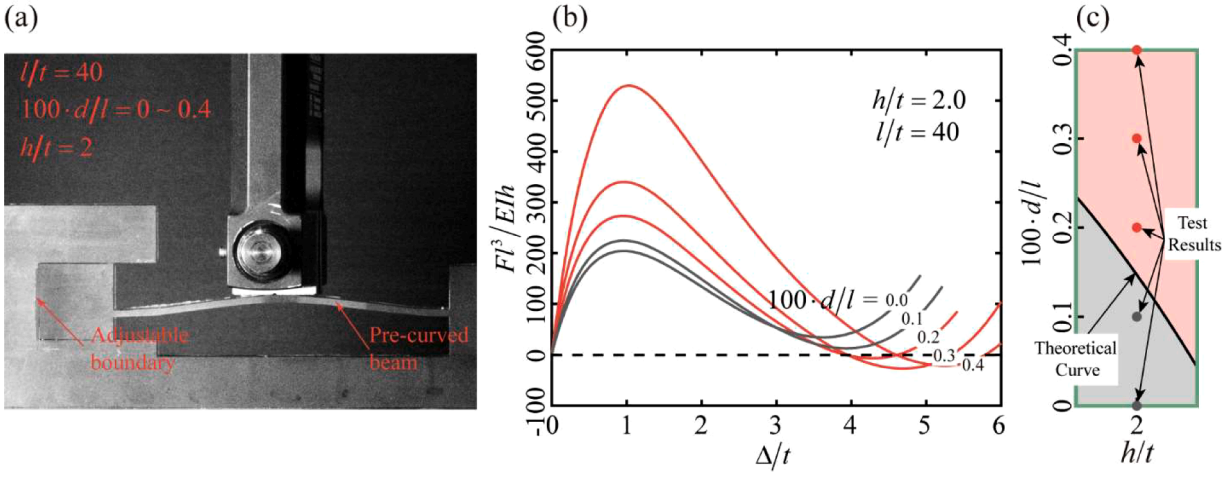

Fig. 11. (a) Fabricated 3D specimen of a curved beam with axial compression and the experimental setup used for mechanical testing. (b) Normalized lateral force–displacement curves obtained from quasi-static experimental tests at various compression levels. (c) Experimental bistability results plotted alongside the theoretical discriminant curve.

An alternative approach achieves switching by changing the compression, which in turn reshapes the potential energy landscape. This stable state switching process involves a complete cycle of decompression and compression, during which three key aspects are monitored: the applied compression (Fig. 12(a)), the center position of the beam (Fig. 12(c)), and the potential energy landscape

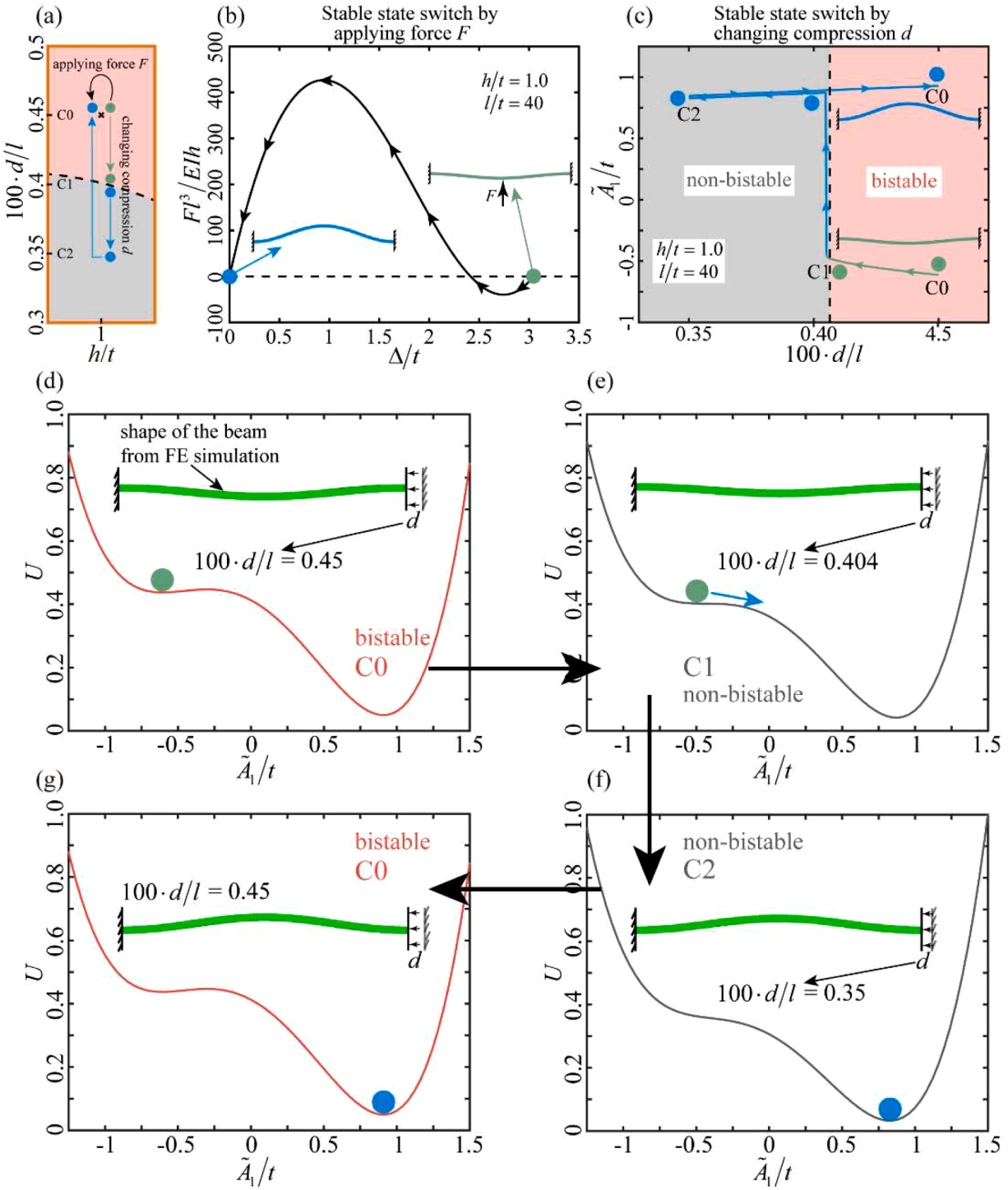

Fig. 12. Stable state switching mechanisms in pre-compressed curved beams. (a) Schematic illustration of two switching methods: one driven by external lateral force, and the other by varying the axial compression. (b) Force–displacement curve and corresponding beam configurations during lateral force–induced switching. (c) Evolution of the beam's $\widetilde{A}_1/t$ during compression-driven switching as d varies. (d-g) Changes in the potential energy landscape and corresponding beam shapes throughout the compression-driven switching process.

(Fig. 12(d–g)). Initially, the beam is compressed to $100\cdot d/l = 0.45$ (denoted as C0) and is set in its secondary stable state, with the midpoint deflected downward ($\widetilde{A}_1/t \approx -0.6$) as shown in Fig. 12(c). The corresponding potential energy landscape is shown in Fig. 12(d), where the potential energy of the secondary state is higher than that of the primary state. As the beam is gradually decompressed, the midpoint moves upward and the energy barrier between the secondary and primary states decreases. When the mpression reaches the critical value of $100 \cdot d/l = 0.404$ (denoted as C1), identified previously as the boundary between the bistable and non-bistable regions, the secondary stable state disappears. Crossing this threshold leads to a rapid release of potential energy, which induces a snap-through motion and causes the center of the beam to shift abruptly upward. Further decompression brings the beam to $100 \cdot d/l = 0.35$ (denoted as C2), where only a single stable state exists, as illustrated in Fig. 12(f). Finally, when the beam is compressed back to the initial C0, the potential energy landscape resumes its original form as shown in Fig. 12(g), but the beam remains in the primary stable state, thus completing the switching process.

This unique stable state switching relies on the tunable and asymmetric bistability of the pre-compressed curved beam, unlike the uncompressed curved beam, whose fixed bistability cannot support the bistable to non-bistable transition, or the compressed straight beam, whose symmetric bistability causes both states to vanish simultaneously during decompression, preventing the selective disappearance of a single stable state, which is essential for enabling the switching process. Therefore, both tunability and asymmetry are essential to achieving stable state switching in the pre-compressed curved beam.

5. Design and demonstration of reprogrammable metasurfaces

The analytical framework developed in the previous sections establishes the bistability criterion that forms the basis for the axial compression–driven stable-state switching mechanism and the metasurface design discussed below. The tunable and asymmetric bistability of the pre-compressed curved beam enables the unique stable state switching. Building on this distinctive property, a coupled pre-compressed curved beam design is proposed as shown in Fig. 13(a) to serve as a unit cell for constructing a 2D programmable metasurface. After fabrication, when the initial shape is fixed ($h/t = 1$ and $l/t = 40$), the bistability of the coupled beam is governed by two key parameters: d_x/l, and d_y/l (compressions along the x and y directions, respectively). For each individual beam, the critical compression is $d/l = 0.404$. Accordingly, the two intersecting lines, $d_x/l = 0.404$ and $d_y/l = 0.404$ shown as blue dashed lines in Fig. 13(b), divide the parameter space into four regions. In the top-right region, both *x*- and *y*-direction beams are bistable, rendering the coupled beams bistable. In the bottom-left region, both beams are non-bistable, resulting in a non-bistable coupled beam. In the top-left and bottom-right regions, one beam is bistable while the other is not, creating an ambiguous condition for bistability. To resolve this, finite element simulations are conducted to assess the bistability of the coupled beams in these mixed regions, with the results showing bistable and non-bistable cases represented by red and gray dots, respectively. The boundary separating the red and gray dots, indicated by the black dashed line in Fig. 13(b), reveals the actual bistability threshold and serves as a discriminant of the coupled beam's bistability.

The coupled beam inherits the tunable and asymmetrical bistability of its component, the compressed curved beam, which enables similar stable state switching from the secondary to the primary state through controlled compression changes. This property can be utilized for metasurface design. As shown in Fig. 14(a), the simplest metasurface is assembled using four coupled beam elements

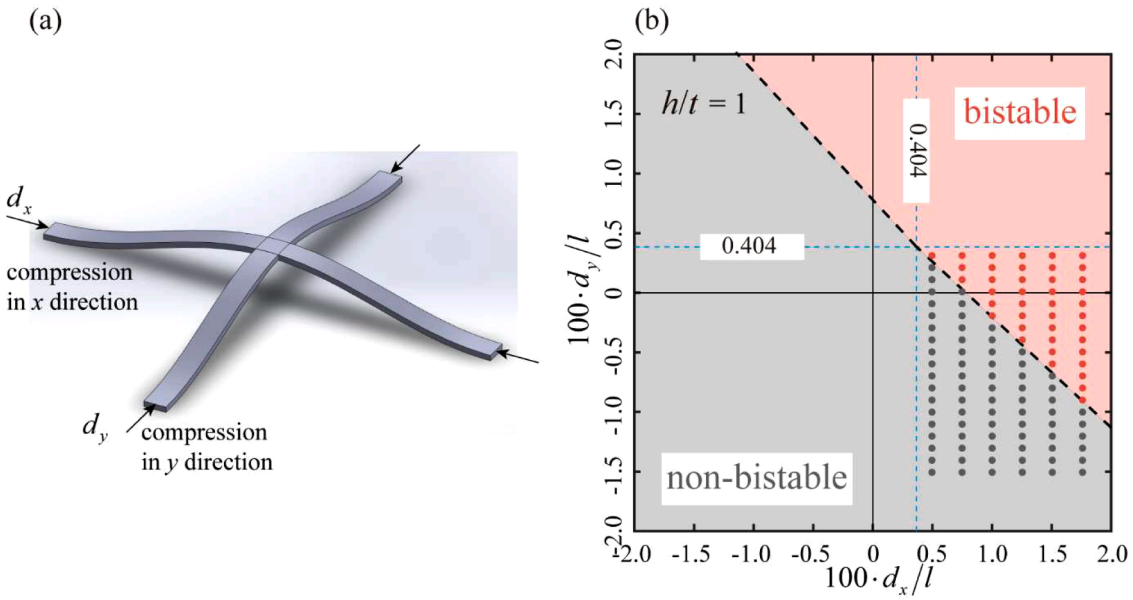

Fig. 13. (a) Schematic diagrams of the coupled beam element. (b) Effect of axial compression applied in both the *x* and *y* directions, d_x/l, and d_y/l, on the bistability of the coupled-beam element, with fixed normalized geometry parameters $h/t = 1$ and $l/t = 40$.

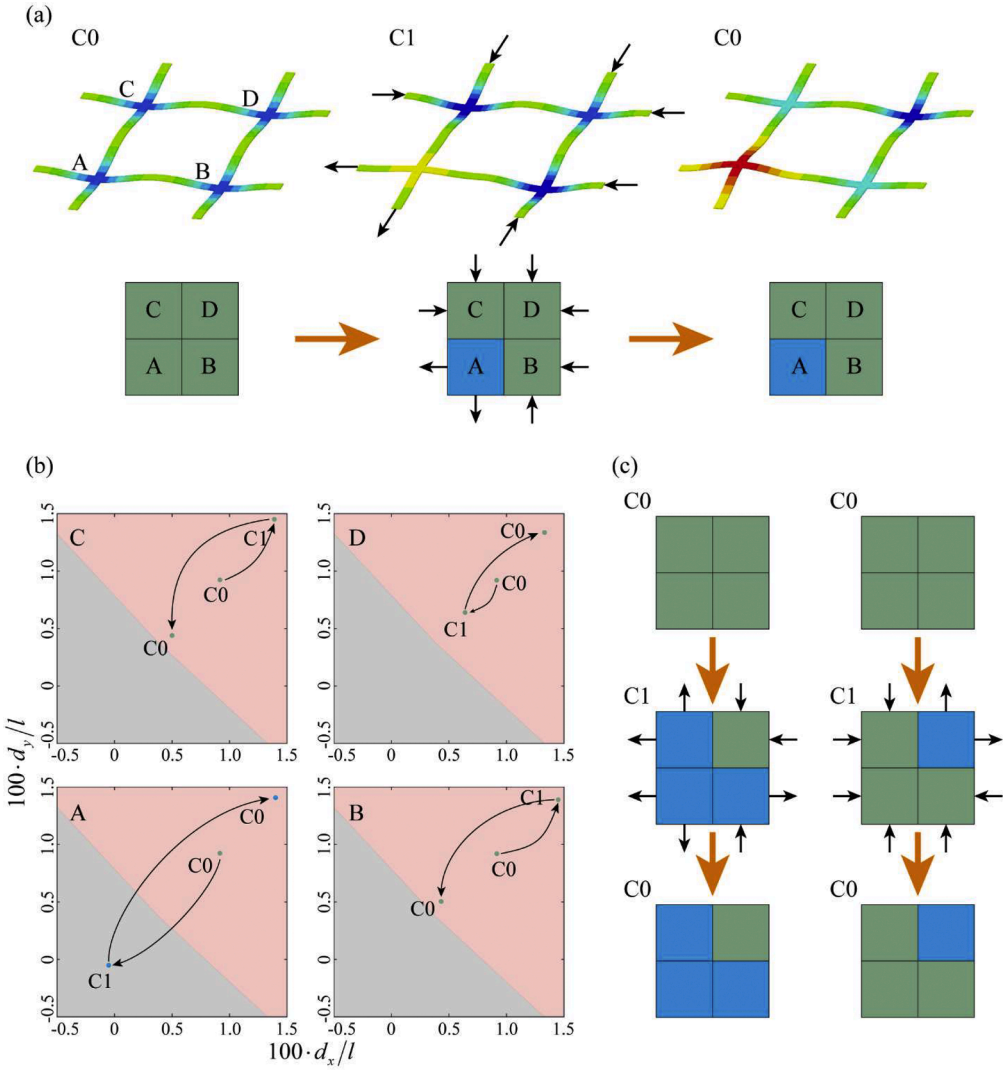

Fig. 14. (a) A 2 × 2 metasurface composed of 4 coupled-beam units programmed via intermediate levels of axial compression. (b) Stable state transitions of the four individual units during the compression-modulation process. (c) Distinct intermediate compression states result in different final metasurface configurations.

labeled A, B, C, and D. The four ends of each element are constrained to lie in the same plane; while they are free to move within the plane, their out-of-plane displacement is restricted. In practice, such grids can be fabricated using the same high-resolution SLA 3D printing technique employed for the specimens in Fig. 11, where the array of coupled-beam units is printed with end structures that are subsequently connected to a surrounding frame. This frame constrains out-of-plane motion while allowing in-plane displacement, consistent with the nodal boundary conditions assumed in our theory and simulations. Similar to previous cases, an initial compression (denoted C0 in Fig. 14(c)) sets all four elements to the bistable regime, with each initially placed in its secondary stable state (bent downward). The color coding indicates the stable state of each element: blue for the primary state and green for the secondary state.

To achieve state switching, an intermediate in-plane load is applied at the boundary of the metasurface, altering the compressive conditions of each element to new values denoted as C1 in Fig. 14(c). For element A, the boundary load significantly reduces its compression, pushing its state into the non-bistable region. As a result, element A transitions upward to its primary state. The other three elements remain within the bistable region and retain their secondary states. Once the intermediate boundary load is removed, stable state switching is achieved: element A remains in its primary state while the others stay unchanged. Each element has two stable states, resulting in a total of 16 possible stable configurations for the 2 × 2 metasurface. By applying different intermediate boundary loads, the compression (C1) for each element can be selectively adjusted. Those elements pushed into the non-bistable region will switch states, enabling programmable control of the metasurface configuration, as illustrated in Fig. 14(c). We also analyze cases where individual elements are directly perturbed. The results show that local perturbations can redistribute in-plane forces and, in certain conditions, trigger selective switching of neighboring elements. The detailed simulation results are provided in the

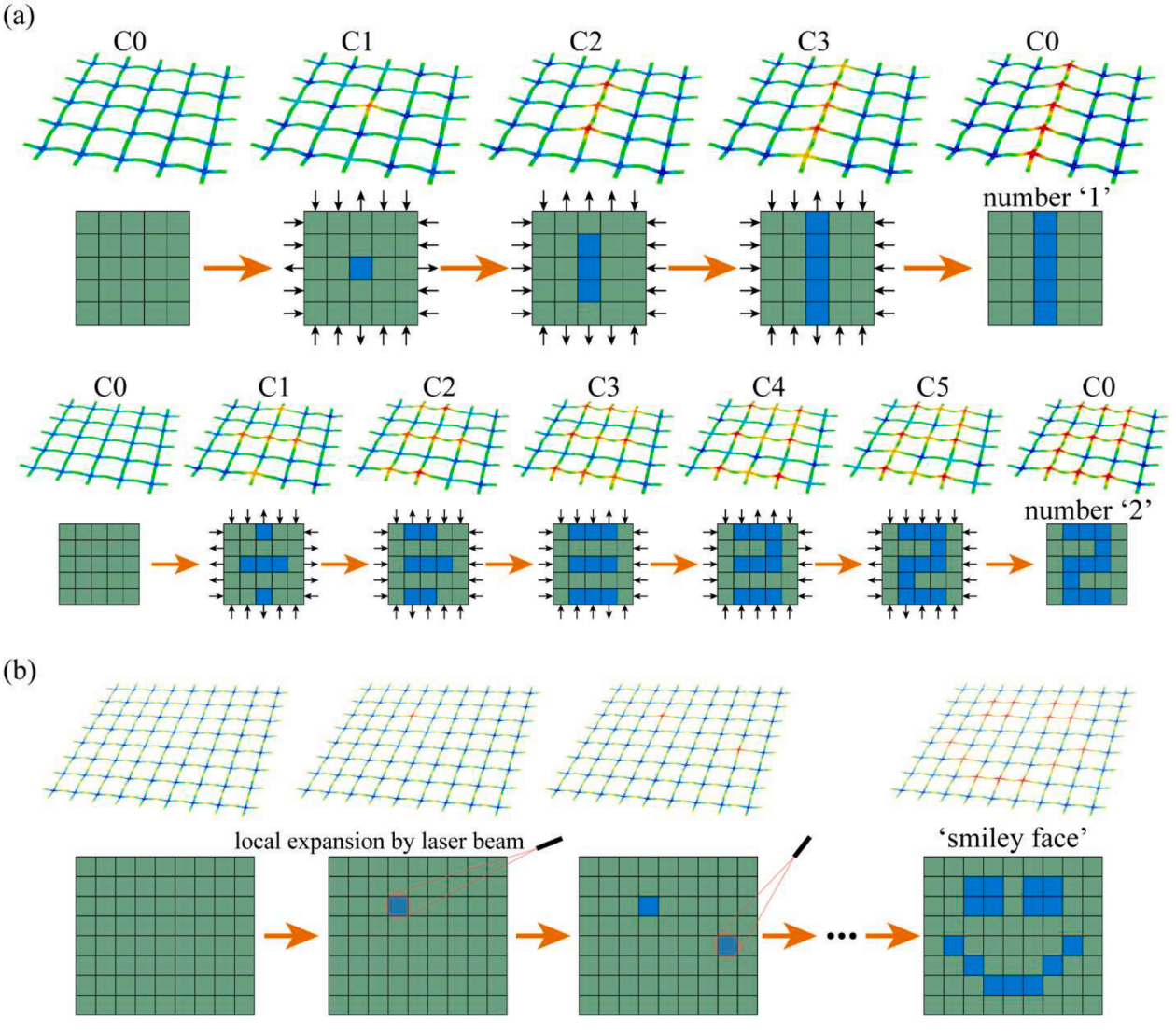

Fig. 15. Larger metasurfaces demonstrating complex programmable configurations (a) Digit-shaped patterns ("1″ and "2″) achieved by applying different sequences of axial compressions to a 5 × 5 metasurface. (b) A smiley-face pattern generated by sequentially applying localized expansion to selected unit cells.

Supplementary Information (Fig. S2).

By expanding the system to a 5 × 5 metasurface, a significantly greater number of configurations can be achieved. Applying boundary loads alters the compression of all elements across the metasurface. With careful tuning of these boundary loads, specific elements intended for state switching can be pushed across the bistability boundary, while others remain within the bistable region to preserve their current states. Fig. 15(a) presents two examples from FEM simulations, where stable state switching of selected elements results in the formation of patterns resembling the numbers "1″ and "2″.

Unlike the earlier 2 × 2 case, where a single intermediate boundary load was sufficient, here multiple boundary loads must be applied sequentially to achieve the desired configuration. Moreover, the order of these loadings can influence the final configuration, as shown in the Supporting Information Fig. S3. Due to the complex and nonlinear relationship between boundary loading and the resulting compression in both the x and y directions, it is challenging to establish a comprehensive guideline for designing arbitrary configurations: an area that needs further investigation.

In larger lattices, creating complex patterns purely through boundary loadings can require carefully designed and often complicated sequences, making selective switching of individual unit cells challenging. It should be noted that this challenge does not imply the theoretical framework cannot be applied to larger systems. The theory remains valid at the unit-cell level, as it can still predict whether a cell is bistable or monostable once the compressions along the x and y directions are specified; the real difficulty lies in arranging boundary compression sequences so that only the intended cells switch while their neighbors remain unaffected.

Local expansion offers a complementary and simpler strategy: it can be regarded as effectively applying a boundary displacement only to targeted unit cells, while leaving the majority of the lattice largely unaffected. For example, Fig. 15(b) illustrates an 8 × 9 metasurface programmed into a “smiley face” configuration by sequentially actuating targeted elements through localized expansion. In practice, such actuation could be achieved by methods such as focused laser heating, where the thermal expansion is confined to a small region and thus induces an effectively anisotropic response.

While our analysis and experiments focus on the quasi-static regime, it is also worth noting that our lattice could, in principle, support dynamical propagation of switching fronts. Such propagation would occur when the entire system is tuned to the verge of stable-state switching, where a local transition redistributes in-plane forces strongly enough to drive neighboring units to switch their stable state, leading to cascaded transitions throughout the lattice. Exploring such dynamic effects would be an interesting direction for future research.

6. Conclusion

This study presents a comprehensive analysis of bistability in beams, highlighting the pre-compressed curved beam as a unique system that combines tunability and asymmetry: two essential features enabling stable state switching. Analytical models, validated through simulations and experiments, define the conditions under which bistability occurs and reveal a discriminant surface separating bistable and non-bistable regimes. Notably, the combination of tunability and asymmetry enables a new switching mechanism: instead of applying a lateral force to overcome the energy barrier between states, the system can be brought from the secondary to the primary stable state by reducing compression and guiding it into the non-bistable region. Leveraging this mechanism, a coupled beam design was proposed as a unit cell for programmable metasurfaces. These units inherit the key properties of their components, allowing controlled state switching through compression changes. Arrays of such beams enable reconfigurable metasurfaces, capable of forming complex patterns through either boundary loading or localized actuation. Beyond the specific geometry studied here, the pre-compressed curved beam, the key result is the identification of a general stable state switching mechanism based on energy barrier elimination and re-formation. The pre-compressed curved beam is used as the simplest demonstration. More broadly, combining geometric asymmetry with tunable compression could inspire new designs that follow the same bistable to monostable to bistable pathway, with potential applications in adaptive structures, shape-morphing devices, and soft robotics. Future work may focus on developing a comprehensive inverse design framework for determining optimal sequential loading paths that reliably achieve targeted state switching, as well as advancing the experimental realization of large-scale metasurfaces.

CRediT authorship contribution statement

Fan Liu: Writing – review & editing, Writing – original draft, Visualization, Validation, Methodology, Investigation, Formal analysis, Data curation, Conceptualization. **Zian Jia:** Methodology, Investigation, Formal analysis. **Xihang Jiang:** Methodology, Investigation. **Lifeng Wang:** Writing – review & editing, Writing – original draft, Validation, Supervision, Resources, Project administration, Methodology, Investigation, Funding acquisition, Formal analysis, Conceptualization.

Declaration of competing interest

The authors declare that they have no known competing financial interests or personal relationships that could have appeared to influence the work reported in this paper.

Supplementary materials

Supplementary material associated with this article can be found, in the online version, at doi:10.1016/j.jmps.2026.106566.

Data availability

Data will be made available on request.

References

Barone, A., Paterno, G., 1982. Physics and applications of the Josephson effect. Wiley, New York.
Cao, T., Hu, T., Zhao, Y., 2020. Research status and development trend of MEMS switches: a review. Micromachines 11, 694.
Cao, Y., Derakhshani, M., Fang, Y., Huang, G., Cao, C., 2021. Bistable structures for advanced functional systems. Adv. Funct. Mater. 31, 2106231.
Chen, Y.Y., Li, T.T., Scarpa, F., Wang, L.F., 2017. Lattice metamaterials with mechanically tunable poisson's ratio for vibration control. Phys. Rev. Appl. 7, 024012.
Chen, T., Bilal, O.R., Shea, K., Daraio, C., 2018. Harnessing bistability for directional propulsion of soft, untethered robots. Proc. Natl. Acad. Sci. 115, 5698–5702.
Chi, Y., Tang, Y., Liu, H., Yin, J., 2020. Leveraging monostable and bistable pre-curved bilayer actuators for high-performance multitask soft robots. Adv. Mater. Technol. 5, 2000370.
Chi, Y., Li, Y., Zhao, Y., Hong, Y., Tang, Y., Yin, J., 2022. Bistable and multistable actuators for soft robots: structures, materials, and functionalities. Adv. Mater. 34, 2110384.
Clark, N.A., Lagerwall, S.T., 1980. Submicrosecond bistable electro-optic switching in liquid crystals. Appl. Phys. Lett. 36, 899–901.
Fu, H., Nan, K., Bai, W., Huang, W., Bai, K., Lu, L., Zhou, C., Liu, Y., Liu, F., Wang, J., 2018. Morphable 3D mesostructures and microelectronic devices by multistable buckling mechanics. Nat. Mater. 17, 268–276.
Ghavidelnia, N., Yin, K., Cao, B., Eberl, C., 2023. Curly beam with programmable bistability. Mater. Des. 230, 111988.
Gorissen, B., Melancon, D., Vasios, N., Torbati, M., Bertoldi, K., 2020. Inflatable soft jumper inspired by shell snapping. Sci. Robot. 5, eabb1967.
Ha, C.S., Lakes, R.S., Plesha, M.E., 2018. Design, fabrication, and analysis of lattice exhibiting energy absorption via snap-through behavior. Mater. Des. 141, 426–437.
Harne, R.L., Wang, K., 2013. A review of the recent research on vibration energy harvesting via bistable systems. Smart Mater. Struct. 22, 023001.
Hua, J., Zhou, Y., Meng, Z., Chen, C.Q., 2025. Pre-compressed beam-based multistable mechanical metamaterials with programmable loading and unloading deformation sequences. Thin-Walled Struct. 209, 112879.
Huang, S.-W., Lin, F.-C., Yang, Y.-J., 2020. A novel single-actuator bistable microdevice with a moment-driven mechanism. Sens. Actuators A: Phys. 310, 111934.
Jeong, H.Y., An, S.C., Seo, I.C., Lee, E., Ha, S., Kim, N., Jun, Y.C., 2019. 3D printing of twisting and rotational bistable structures with tuning elements. Sci. Rep. 9 (1), 324.
Jia, Z., Liu, F., Jiang, X.H., Wang, L.F., 2020. Engineering lattice metamaterials for extreme property, programmability, and multifunctionality. J. Appl. Phys. 127, 15.
Jia, Z., Liu, F., Li, L., Wang, L.F., 2022. Elastic anisotropy and wave propagation properties of multifunctional hollow sphere foams. Compos. Struct. 291, 115540.
Leanza, S., Zhao, R.R., Hutchinson, J.W., 2024. The elastica with pre-stress due to natural curvature. J. Mech. Phys. Solids 190, 105690.
Li, T.T., Hu, X.Y., Chen, Y.Y., Wang, L.F., 2017. Harnessing out-of-plane deformation to design 3D architected lattice metamaterials with tunable Poisson's ratio. Sci. Rep. 7, 8949.
Lisman, J.E., 1985. A mechanism for memory storage insensitive to molecular turnover: a bistable autophosphorylating kinase. Proc. Natl. Acad. Sci. 82, 3055–3057.
Liu, F., Jiang, X.H., Wang, X.T., Wang, L.F., 2020. Machine learning-based design and optimization of curved beams for multistable structures and metamaterials. Extreme Mech. Lett. 41, 101002.
Liu, M., Domino, L., de Dinechin, I.D., Taffetani, M., Vella, D., 2023a. Snap-induced morphing: from a single bistable shell to the origin of shape bifurcation in interacting shells. J. Mech. Phys. Solids 170, 105116.
Liu, Y., Pan, F., Xiong, F., Wei, Y., Ruan, Y., Ding, B., Yang, K., Chen, Y., 2023b. Ultrafast shape-reconfigurable chiral mechanical metamaterial based on prestressed bistable shells. Adv. Funct. Mater. 33, 2300433.
Pal, A., Sitti, M., 2023. Programmable mechanical devices through magnetically tunable bistable elements. Proc. Natl. Acad. Sci. 120, e2212489120.
Percy, J.J., Kanthamani, S., 2023. Revolutionizing wireless communication: a review perspective on design and optimization of RF MEMS switches. Microelectron. J. 139, 105891.
Qiu, J., Lang, J.H., Slocum, A.H., 2004. A curved-beam bistable mechanism. J. Microelectromechanical Syst. 13, 137–146.
Shan, S., Kang, S.H., Raney, J.R., Wang, P., Fang, L., Candido, F., Lewis, J.A., Bertoldi, K., 2015. Multistable architected materials for trapping elastic strain energy. Adv. Mater. 27, 4296–4301.
Silverberg, J.L., Na, J.-H., Evans, A.A., Liu, B., Hull, T.C., Santangelo, C.D., Lang, R.J., Hayward, R.C., Cohen, I., 2015. Origami structures with a critical transition to bistability arising from hidden degrees of freedom. Nat. Mater. 14, 389–393.
Timoshenko, S.P., Gere, J.M., 2012. Theory of elastic stability, 2nd ed. Courier Corporation, New York.
Vangbo, M., Bäcklund, Y., 1998. A lateral symmetrically bistable buckled beam. J. Micromech. Microeng. 8, 29.
Vangbo, M., 1998. An analytical analysis of a compressed bistable buckled beam. Sens. Actuators A: Phys. 69, 212–216.
Vasios, N., Deng, B., Gorissen, B., Bertoldi, K., 2021. Universally bistable shells with nonzero Gaussian curvature for two-way transition waves. Nat. Commun. 12, 695.
Wang, C., Guo, H., Liu, R., Deng, Z., Chen, Y., You, Z., 2024. Reconfigurable origami-inspired multistable metamorphous structures. Sci. Adv. 10, eadk8662.
Xia, Y., Ruzzene, M., Erturk, A., 2020. Bistable attachments for wideband nonlinear vibration attenuation in a metamaterial beam. Nonlinear Dyn. 102, 1285–1296.
Yan, W., Yu, Y., Mehta, A., 2019. Analytical modeling for rapid design of bistable buckled beams. Theor. Appl. Mech. Lett. 9, 264–272.
Yasuda, H., Johnson, K., Arroyos, V., Yamaguchi, K., Raney, J.R., Yang, J., 2022. Leaf-like origami with bistability for self-adaptive grasping motions. Soft Robot. 9, 938–947.